

Instabilities in the flow between co- and counter-rotating disks

By G. GAUTHIER[†], P. GONDRET, F. MOISY
AND M. RABAUD

Laboratoire FAST, Bât. 502, Campus Universitaire, F-91405 Orsay Cedex, France

(Received 20 November 2001 and in revised form 22 April 2002)

The flow between two rotating disks (radius to height ratio of 20.9), enclosed by a rotating cylinder, is investigated experimentally in the cases of both co- and counter-rotation. This flow gives rise to a large gallery of instability patterns. A regime diagram of these patterns is presented in the (Re_b, Re_t) -plane, where $Re_{b,t}$ is the Reynolds number associated with each disk. The co-rotation case and the weak counter-rotation case are very similar to the rotor–stator case, both for the basic flow and the instability patterns: the basic flow consists of two boundary layers near each disk and the instability patterns are the axisymmetric vortices and the positive spirals described in the rotor–stator experiments of Gauthier, Gondret & Rabaud (1999), Schouveiler, Le Gal & Chauve (2001), and the numerical study of Serre, Crespo del Arco & Bontoux (2001). The counter-rotation case with higher rotation ratio is more complex: above a given rotation ratio, the recirculation flow becomes organized into a two-cell structure with the appearance of a stagnation circle on the slower disk. A new kind of instability pattern is observed, called *negative spirals*. Measurements of the main characteristics of this pattern are presented, including growth times, critical modes and phase velocities.

1. Introduction

The flows above or between infinite rotating disks are known as generalized von Kármán (1921) swirling flows. They have been the subject of many studies, both fundamental and applied. The reasons for this interest are multiple. First, this is a three-dimensional flow with an exact self-similar solution which gives rise to a very rich class of instability patterns. Secondly, this is a model geometry for turbomachinery, hard disk drive and geophysical flows. Most of the studies deal with the flow over a rotating disk, or between a stationary and a rotating disk (rotor–stator configuration), and only few authors have studied the case when both disks rotate. The first studies of the stability of the flow over an infinite rotating disk are those by Gregory, Stuart & Walker (1955) and Faller & Kaylor (1966). They both deal with the stability of the boundary layer over an infinite rotating disk. These authors report two types of instabilities leading to spirals patterns. The first pattern, denoted class A (or type II), is due to a viscous instability while the second one, denoted class B (type I) comes from an inflectional instability.

The first studies of the two-disks problem are due to Batchelor (1951) and Stewartson (1953). In the case of a rotating and a fixed disk, Batchelor showed that the flow

[†] Permanent address: Laboratoire de Mécanique de Lille (URA 1441), bd P. Langevin, Cité Scientifique 59655 Villeneuve d'Ascq cedex, France.

consists of two boundary layers separated by a core in solid-body rotation. For disks in exact counter-rotation, Batchelor argued that the flow will be also constituted by two boundary layers but the core will be separated into two parts rotating in opposite directions separated by a transition layer. According to Stewartson, in both cases the core remains at rest. In fact, as showed by Rogers & Lance (1960) and many others later (see Zandbergen & Dijkstra (1987)), Batchelor and Stewartson flows are two of several solutions that progressively appear as the Reynolds number is increased. In the real case of disks of finite radius Brady & Durlofsky (1987) showed that this degeneracy can be removed by the end condition. Dijkstra & van Heijst (1983) showed numerically and experimentally the coexistence of a Stewartson type flow and a Batchelor type flow for counter-rotating disks. The Stewartson type flow holds near the centre while the Batchelor type flow is limited to the periphery of the disks. This result was confirmed by Brady & Durlofsky (1987) and more recently by Lopez (1998). The first study which deals with the stability of the counter-rotating flow is due to Szeri *et al.* (1983). These authors present results for exact counter-rotation at a fixed angular velocity Ω for an aspect ratio $R/h > 10$. The flow is described in terms of the local Reynolds number ($Re_l = \Omega r^2/\nu$) since different structures appear at different radial locations. They reported the existence of spirals and concentric structures, respectively for $Re_l \geq 552$ and $Re_l \geq 960$. These instabilities are limited to the boundary layers close to disks while the core remains stable. Recently, Lopez *et al.* (2002) addressed, both experimentally and numerically, the issue of the stability and the pattern formation in the flow between two counter-rotating disks, not limited to exact counter-rotation. Their study is limited to one Reynolds number (here based on the gap h between the disks $Re_h = \Omega h^2/\nu = 250$) and one aspect ratio ($R/h = 2$), with a rotation ratio ranging from 0 to -1 , and present extensive results of the stability of the flow. They report new instabilities leading to an azimuthal modulation of wavenumber 4 and 5 due to a supercritical Hopf bifurcation. Contrary to the structures observed by Szeri *et al.* (1983) this pattern is not limited to the disk boundary layers but fills the whole cell. The successive bifurcations in the exact counter-rotation case for an aspect ratio $R/h = 1/2$ have been recently investigated by Nore *et al.* (2003). The study presented here, for a much higher aspect ratio ($R/h = 20.9$), extends from counter-rotating to co-rotating configurations and explores both boundary layer and shear instabilities.

The main goal of this paper is to investigate the onset and the nature of the flow instabilities. The different patterns are presented in a so-called ‘regime diagram’, where the two control parameters are the Reynolds number based on each disk rotation rate. In §2 we present the experimental set-up and the visualization technique. Then §3 is devoted to the basic laminar flow, emphasizing the measurement methods of the boundary layer thickness and the stagnation circle. Section 4 presents the regime diagram of the flow between two rotating disks and a detailed study of the three kinds of instability patterns.

2. Experimental set-up

The experimental set-up is the same as the one described in detail in Gauthier, Gondret & Rabaud (1999). The cell, sketched in figure 1, consists of a cylinder of small height h closed by a top disk and a bottom disk, both of radius $R = 140$ mm. The upper disk is made of glass and rotates together with the cylindrical sidewall which is made of PVC. The bottom disk is made of rectified brass, with a black coating to improve visualization contrast. To allow differential rotation the radius

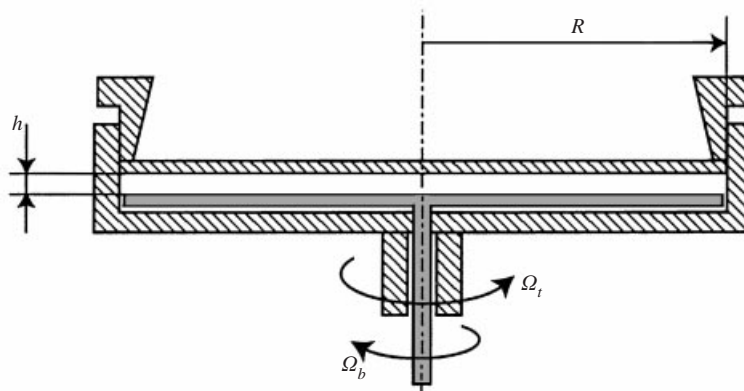


FIGURE 1. Sketch of the experimental set-up.

of the bottom disk is slightly smaller (a tenth of millimetre) than the radius of the shrouding cylinder. The thickness of the cell has been fixed at $h = 6.7$ mm for the present study, corresponding to an aspect ratio $R/h = 20.9$. *In situ* measurements show that the thickness h is constant within ± 0.17 mm (i.e. 2.5%) when both disks are rotating. Each disk rotation is controlled by a DC motor with a tachometric generator and a regulation loop. After two speed reducers, angular velocities Ω_i ($i = b, t$ for bottom and top disk) range from 0 to 10 rad s^{-1} . Positive angular velocity is chosen anticlockwise when seen from above and in all the figures presented hereafter, the top disk has a positive angular velocity, whereas the bottom disk has either a positive (co-rotation) or negative (counter-rotation) angular velocity.

Two visualization techniques are used to explore the flow structure. The first one consists of a concentric circular light source and a CCD camera located along the disk axis. In the second technique, the light source consists of a laser sheet located in a plane containing the radial and the axial directions (meridian plane), and a camera with a macro lens is located close to the upper disk, with an orientation of 45° to the laser sheet. The resulting images thus have different horizontal and vertical scales. In both cases the images are digitized on a 8 bit acquisition board and processed with the freeware NIH Image[†]. More details about the set-up can be found in Gauthier (1998).

The cell is filled with a mixture of water, anisotropic flakes (3% of Kalliroscope[‡]) and glycerol. The glycerol concentration was varied, so that the kinematic viscosity lies in the range $1.0 \times 10^{-6} < \nu < 8 \times 10^{-6} \text{ m}^2 \text{ s}^{-1}$ at 20°C . In both the visualization techniques previously described, we observe the light reflected by the flakes. Information such as the wavelength or phase velocity of the structures, or the boundary layer thickness, can be extracted from the spatial variation of the reflected light. On the other hand, such visualization techniques do not allow one to extract more quantitative information about the velocity field. We have shown in a previous study (Gauthier, Gondret & Rabaud 1998) that, in three-dimensional flows, the light intensity is due to flakes rotating in a manner that depends on the local velocity gradient tensor of the flow. However, in the particular case of the rotating disk flow, we have also shown that the boundary layer appears as a bright line in the radial laser sheet visualization. The global light intensity was shown to be proportional to the particle concentration as long as interactions between flakes can be neglected. However, even

[†] Internet address: <http://rsb.info.nih.gov/nih-image/download.html>

[‡] Kalliroscope Corporation, 264 Main Street, Box 60, Groton, MA 01450, USA.

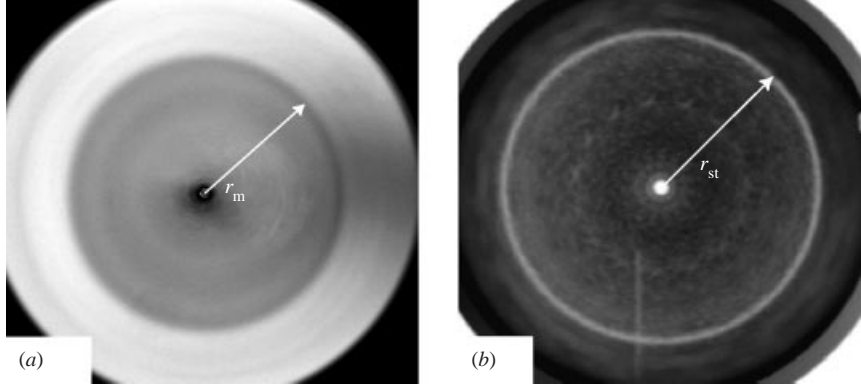


FIGURE 2. (a) Visualization of the merging radius r_m from intensity contrast for $Re_t = 75$, $Re_b = -10.2$. (b) Visualization of the stagnation radius r_{st} by settled particles on the slower (bottom) disk, for $Re_t = 50$, $Re_b = -16$.

though the proportionality between the light variation from the flow patterns and the perturbed velocity field is not proved we will assume, as usual, such a relation.

In order to characterize the flow, one has to choose among several dimensionless numbers constructed from the relevant parameters R , h , ν , Ω_b and Ω_t . In the case of a single infinite disk rotating at Ω , the only lengthscale is the boundary layer thickness $\delta_0 = (\nu/\Omega)^{1/2}$ (Ekman 1905). In this case, the only dimensionless number is the local Reynolds number defined as the ratio of the local radius r to the thickness δ_0 (Greenspan 1968). When both disks are rotating, we choose, like Dijkstra & van Heijst (1983), two Reynolds numbers based on the thickness of the cell: $Re_t = \Omega_t h^2 / \nu$. We also make use of another non-independent dimensionless number, the rotation ratio $s = \Omega_b / \Omega_t$ (with $|s| \leq 1$ since all the results presented here correspond to $|\Omega_b| \leq \Omega_t$); since the boundary layer thickness of each disk is found to depend essentially on the faster-disk angular velocity, the set of parameters (Re_t, s) is sometimes more convenient than (Re_t, Re_b) . We note that $s > 0$ for the co-rotation case (both disks rotating anticlockwise) and $s < 0$ for the counter-rotation case, $s = 0$ corresponding to the rotor/stator case. Finally, the third dimensionless number is the aspect ratio of the cell R/h . For the present study it has been kept constant, $R/h = 20.9$.

3. Basic laminar flow

We first focus on the basic laminar flow, both in the co- and counter- rotation cases, using visualizations from above and from meridian laser sheets. For small rotation rates no time or azimuthal variation of the reflected light can be seen (see figure 2a), so that the basic flow is axisymmetric and stationary. This basic flow can be described in terms of its azimuthal (primary flow) and meridian components (secondary recirculating flow).

3.1. Azimuthal flow

We first describe the basic laminar flow in terms of its azimuthal component. Each disk tends to impose its rotation, leading to an essentially azimuthal velocity field. This structure can be characterized from visualizations of the anisotropic flakes from above and in the meridian plane. Laser sheet visualizations presented in figure 3 show

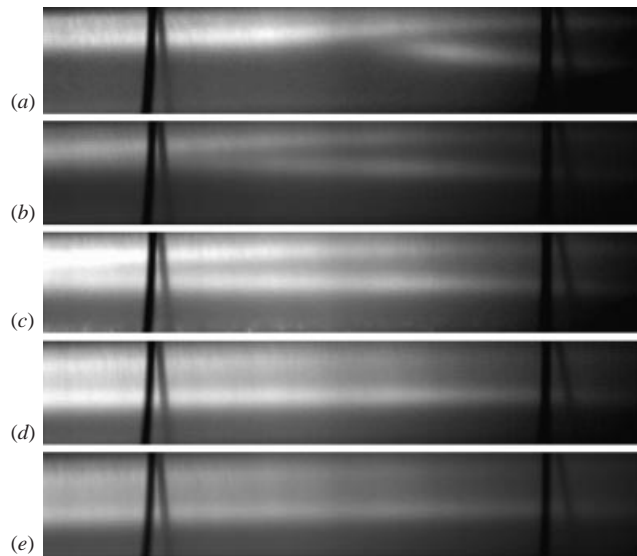


FIGURE 3. Radial laser sheet visualizations of the laminar basic flow at $Re_t = 89$ for increasing rotation rate of the bottom disk, from counter- to co-rotation: (a) $s = -0.2$; (b) $s = -0.1$; (c) $s = 0$; (d) $s = 0.11$; (e) $s = 0.3$. The two mainly horizontal bright strips correspond to the faster- (upper) and slower- (lower) disk boundary layers. In each picture, the faster-disk boundary layer does not evolve while the slower-disk one becomes more horizontal as the rotation ratio is increased. The pictures represent the whole gap of the cell (the top and bottom bounds of the figure correspond to the top and bottom disks, $h = 6.7$ mm apart) but only a part of its radial extent. The centre is on the left and the vertical black lines, drawn for measuring purposes, correspond respectively to radial locations $r \approx 100$ mm and $r \approx 115$ mm.

the structure of the flow in the meridian plane, for five rotation ratios from counter- to co-rotation (from $s = -0.2$ to $s = 0.3$). On each picture, one can see two bright strips, one close to the top disk and the other one close to the bottom disk. As shown in a previous study (Gauthier *et al.* 1998), these bright strips correspond to boundary layers that develop on each disk, providing a measurement of the boundary layer thickness. (We note here that the boundary layer developing over the shrouding cylinder cannot be visualized with our experimental set-up). The boundary layer attached to the faster (top) disk is similar to the one observed over an infinite rotating disk. Its thickness δ_t does not depend on r , and depends only on the top Reynolds number: $\delta_t \approx 2.2(\nu/\Omega_t)^{1/2}$, as in our rotor–stator study. On the other hand, the boundary layer attached to the bottom (slower) disk is only observed for large enough radius, and its thickness evolves with r and reaches the upper boundary layer at a given radius, denoted r_m (merging radius). Here again this observation agrees with our rotor–stator experiment. This thickness δ_b , shown in figure 4 for $Re_t = 89$, essentially depends on the top Reynolds number. Moreover, the bottom-disk boundary layer becomes more horizontal as the rotation ratio is increased from counter-rotation to co-rotation. In the co-rotation case, these observations are in agreement with the recent numerical simulations of Lopez (1998) with a similar set-up but with a smaller aspect ratio $R/h = 2$ (see figure 3 of Lopez 1998).

The non-constant thickness of the bottom boundary layer has important consequences for the global structure of the flow, as can be seen from visualization from above (figure 2a). The light reflected by the anisotropic flakes is much brighter in the outer ring than in the central region of the flow. The intensity jump, located here at

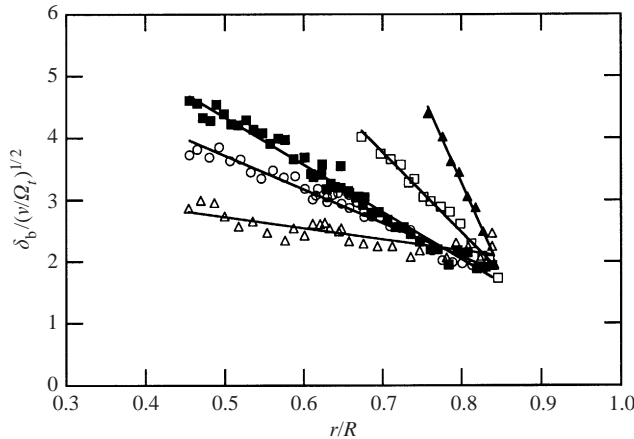


FIGURE 4. Boundary layer thickness of the (slower) bottom disk as a function of the radial position and for increasing rotation ratios for $Re_t = 89$. \blacktriangle , $s = -0.2$; \square , $s = -0.1$; \blacksquare , $s = 0$; \circ , $s = 0.3$; \triangle , $s = 0.87$.

$r = 73$ mm ($r/R = 0.52$), is rather sharp (confined to a width $\simeq 0.02R$), suggesting that a strong change in the flow structure occurs at this location. The location of this change is found to correspond to the radius of merging of the boundary layers observed in figure 3. The intensity jump can be understood from the dynamics of alignment of the anisotropic flakes. In the central part of the flow ($r < r_m$), the reflected light is weak, suggesting that the flakes do not have a well-defined orientation. This is in agreement with the torsional Couette flow described by Sirivat (1991), since for a Couette flow the particles do not have a defined orientation (Savas 1985). On the other hand, in the outer part of the flow ($r > r_m$), the light intensity is much stronger, indicating that the flakes have mainly reached a direction parallel to the disks. This situation now corresponds to a separate boundary layer flow, in which the larger axis of the flakes becomes approximately oriented along the direction of the positive strain rate, as shown by Gauthier *et al.* (1998). Beyond this merging radius, separated boundary layers appear on each disk with a core in quasi-solid-body rotation: the flow is of Batchelor type (sketched in figure 5).

Measurements of the merging radius r_m , from the light intensity change from above, are shown in figure 6 as a function of the top Reynolds number Re_t for different bottom Reynolds numbers ($Re_b = -20, -15, -10$ and -5). The Re_b dependence of r_m is weak, since the bottom boundary layer thickness δ_b is essentially controlled by the rotation of the top disk. As the top Reynolds number is increased, r_m decreases and the torsional Couette part of the flow is confined to a smaller radius. This decrease can be recovered from the results of figure 4: since both boundary layer thicknesses δ_b and δ_t scale as $(\nu/\Omega_t)^{1/2}$ and δ_b decreases linearly with r , we can deduce that the merging of the two boundary layers occurs at a radial location $r_m \simeq A - B Re_t^{1/2}$ (where A and B depend on Re_b and on the details of the slower disk boundary layer profile). This is indeed the case, as shown in figure 6. Note that the merging radius also exists in rotor–stator and weak co-rotation, but the weakness of the intensity contrast in the central part of the flow does not allow reliable measurements of r_m in this case (uncertainty is of order $0.1R$).

As we will see, the transition in the azimuthal profile occurring at r_m is found to play an important role in the bifurcated flow, especially for the onset of the positive spirals (discussed in §4.2).

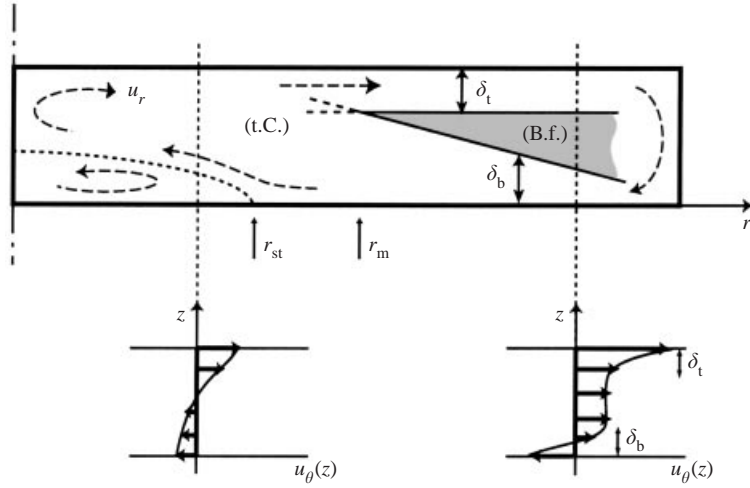


FIGURE 5. Sketch of the flow structure in a meridian plane, and typical azimuthal velocity profiles at two radial locations: δ_t and δ_b are respectively the thickness of the faster- (top) and slower- (bottom) disk boundary layers; r_{st} and r_m denote the stagnation radius and the merging radius respectively. The dashed lines represent the radial recirculating flow in the particular case where the two-cell structure is present (for $s < -0.2$). t.C. denotes torsional Couette, and B.f. Batchelor flow.

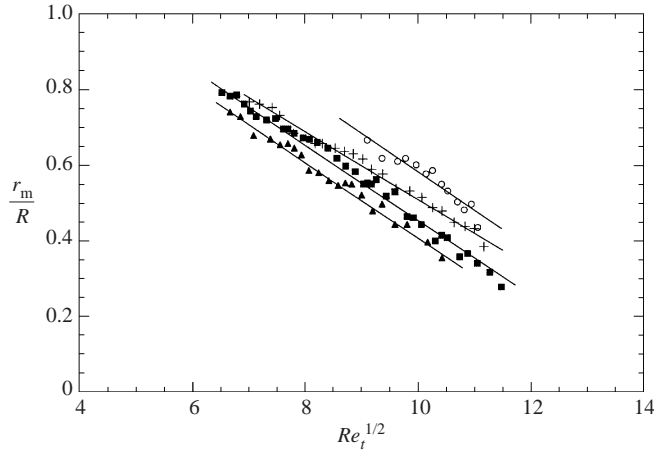


FIGURE 6. Merging radius r_m as a function of $Re_t^{1/2}$ for: \circ , $Re_b = -20$; $+$, $Re_b = -15$; \blacksquare , $Re_b = -10$; \blacktriangle , $Re_b = -5$. The experimental uncertainty is $\simeq 0.02R$, roughly of the size of the symbols. Lines are best fits with $r_m \simeq A - B Re_t^{1/2}$.

3.2. Recirculating flow

Each rotation is associated with a meridian recirculating flow, which can be inward or outward depending on the rotation ratio. For arbitrary positive or small negative rotation ratio s , the radial recirculating flow is roughly the same as in the rotor–stator case: it consists of an outward boundary layer close to the faster disk and an inward boundary layer close to the slower disk. In the counter-rotating case, as the rotation ratio s is decreased below -0.2 , the radial recirculating flow appears to become organized into a two-cell recirculating structure, as shown by Dijkstra & van Heijst (1983). The centrifugal flow induced by the faster disk recirculates towards the centre of the slower disk due to the lateral endwall. This inward recirculation flow meets the

outward radial flow induced by the slower disk, leading to a stagnation circle where the radial component of the velocity vanishes (figure 5).

Measurements of the stagnation circle radius r_{st} have been performed following a procedure similar to the one described by Dijkstra & van Heijst (1983): small Nylon particles, 130 μm in diameter and slightly more dense than the fluid ($\rho_p \simeq 1.06 \text{ kg m}^{-3}$), settle and accumulate on a stagnation circle on the slower (bottom) disk, as shown in figure 2(b). This accumulation is mainly due to radial motion of particles that have already settled on the bottom disk. So for the accumulation to be possible, the radial component of the flow has to be strong enough at the height of the particle diameter in order to counteract the wall friction. Particles of radius r_p at rest experience a Stokes drag force $F_d = 6\pi\rho_f\nu r_p U$ (where ρ_f is the fluid density and U the fluid velocity modulus) balanced by the static wall friction $F_f = (4/3)\pi r_p^3 \delta\rho g \mu_s$ (where μ_s is the static friction coefficient and $\delta\rho = \rho_p - \rho_f$ is the specific particle density). This gives a fluid velocity threshold for the particle motion,

$$U \geq \mu_s \frac{2}{9} \frac{g r_p^2 \delta\rho}{\nu \rho_f},$$

where the velocity modulus U has to be chosen at height $z \simeq r_p$. Since our typical boundary layer thickness $\delta_b \simeq (\nu/\Omega_t)^{1/2}$ is larger than the particle size, this velocity is expected to be of order $\Omega_t R r_p / \delta_b$, leading to a threshold for the top Reynolds number of order

$$Re_t \simeq h^2 \frac{(\mu_s g \delta\rho / \rho_f)^{2/3}}{\nu^{4/3}}.$$

For a given kinematic viscosity ν , this procedure allows us to measure r_{st} only down to some threshold $Re_t \sim \nu^{-4/3}$ (typically $Re_t \simeq 10\text{--}20$). So high viscosities are required to obtain reliable measurements of low values of the stagnation radius; otherwise, the measured radius overestimates the actual one. On the other hand, we also observe that large velocities prevent the stability of the particle accumulation, so that low viscosities are needed in order to measure the large values of r_{st} . Finally, a given viscosity allows reliable measurements of r_{st} using the sedimentation method only for a limited range of Reynolds numbers.

Figure 7 shows r_{st} as a function of the rotation ratio $-s$ for two top Reynolds numbers. Each curve is a collection of measurements performed at different viscosities, for the reason explained above. The stagnation radius r_{st} is found to be smaller than r_m confirming the difference between the azimuthal and radial two-cell structures. For larger $|s|$, the difference between r_{st} and r_m is found to decrease, in agreement with the observation of Dijkstra & van Heijst (1983) that the radial recirculation cells tend to coincide with the azimuthal cells in the limit $s \rightarrow -1$. Figure 7 suggests that a critical value of s , around -0.2 , has to be reached in order to obtain the two-cell recirculation structure. The stagnation circle is not observed in the co-rotating case, unlike the merging radius that exists both for $s < 0$ and $s > 0$. We note that reliable measurements of r_{st} are difficult to obtain for small rotation ratio ($r_{st}/R < 0.4$), because of the weakness of the recirculating radial flow attached to the slower disk and of the possible screening effect due to the accumulation of particles at small radius. Such a critical value of s has also been found by Dijkstra & van Heijst (1983), and can be interpreted in terms of a balance between the inward and outward flow over the slower disk. These results show that a given value of r_{st} is obtained essentially at a fixed rotation ratio s , regardless of the Reynolds number magnitude. However, the five curves of equal r_{st}/R plotted in the $(-Re_b, Re_t)$ -plane of figure 8

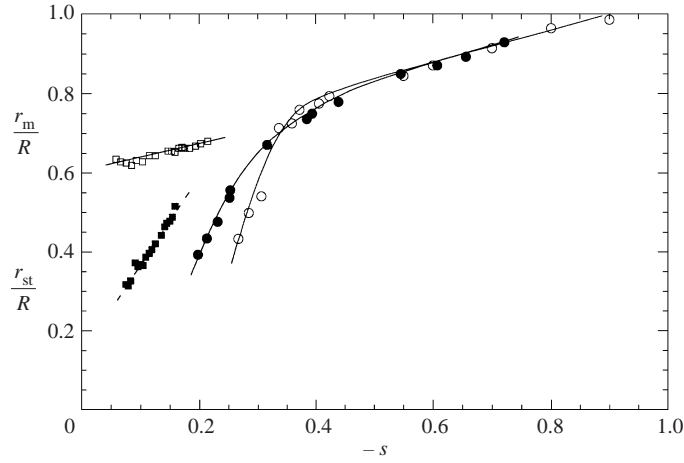


FIGURE 7. Stagnation radius r_{st} (circles) and merging radius r_m (squares) as a function of the rotation ratio $-s$ (counter-rotation), for $Re_t = 50$ (open symbols) and $Re_t = 100$ (filled symbols). The range of measurements for r_m is limited by the appearance of disorder at $Re_b < -18$.

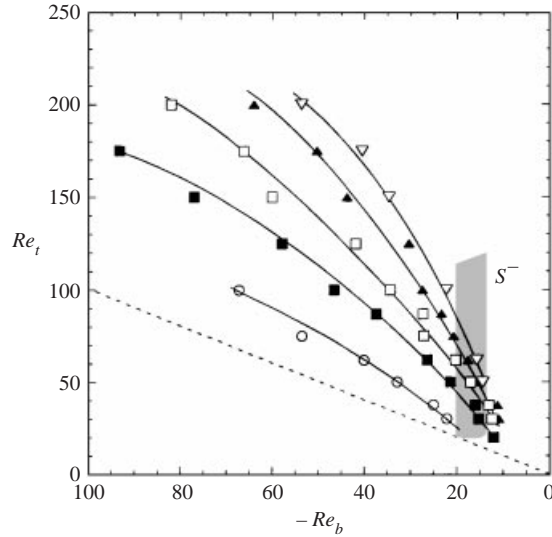


FIGURE 8. Isovalues of the stagnation radius r_{st} in the Reynolds number plane Re_t, Re_b . \circ , $r_{st}/R = 0.9$; \blacksquare , $r_{st}/R = 0.8$; \square , $r_{st}/R = 0.7$; \blacktriangle , $r_{st}/R = 0.6$; ∇ , $r_{st}/R = 0.5$. The grey zone corresponds to the region of existence of the negative spirals (see §4.3), and the dashed line to the exact counter-rotation. Continuous lines are guides for the eye.

show significant departures from straight lines at high Reynolds number, i.e. similarity does not hold on the whole range of Reynolds numbers covered here. Surprisingly figure 8 shows that the stagnation circle is not only a property of the axisymmetric basic flow, but remains visible even in the presence of structures such as negative spirals (see §4.3) or turbulence. From figure 7, it appears that r_m and r_{st} are never observed simultaneously. However, this is due to difficulties in observing large values of r_m in the presence of instabilities (§4.3).

4. Instability patterns

We now turn to the instability patterns of the flow between two rotating disks close to each other ($R/h = 20.9$), in both co- and counter-rotating flows. A gallery of the different patterns described below is shown on figure 9.

For $s \geq 0$ (rotor–stator or co-rotation) and Re_b fixed, on increasing Re_t , propagating circular structures (denoted C) are first observed (figure 9a). These axisymmetric vortices appear close to the cylindrical wall, propagate towards the centre and disappear before reaching the merging radius r_m . Above a secondary threshold of Re_t , spiral structures appear at the periphery of the disks, and circles remain confined between two critical radii (figure 9e). These spirals are called *positive spirals* (denoted S^+) since they roll up to the centre in the direction of the faster disk (here the top one). Increasing Re_t further, positive spirals progressively invade the whole cell. Still increasing Re_t , the flow becomes more and more disordered (denoted D , figure 9d).

For $s < 0$ (counter-rotating case) the onset of the instability patterns depends on the Reynolds numbers of both disks. For low bottom Reynolds number, $-11 < Re_b < 0$, on increasing the Reynolds number of the upper disk, the appearance of the instability patterns is the same as in the rotor–stator or co-rotation case: axisymmetric propagating vortices, positive spirals and disorder. But, for $-18 < Re_b < -11$, spirals of a new kind appear on increasing Re_t . These spirals are said to be *negative* (and denoted S^-) since they now roll up to the centre in the direction of the slower counter-rotating disk (figure 9c). Unlike circles and positive spirals, negative spirals extend from the periphery to the centre. Increasing Re_t further, positive spirals appear as well at the periphery of the disk, as can be seen in figure 9(f). Here negative and positive spirals seem to coexist without strong interaction. Still increasing Re_t , negative spirals disappear and positive spirals alone remain (figure 9b). Increasing Re_t yet further, circles appear as in the co-rotation case. Still increasing Re_t , the structures become disorganized and the flow becomes turbulent. For $Re_b < -18$ the negative spirals described above become wavy, the flow is more and more disorganized and continuously becomes turbulent without a well-defined threshold. Depending on the Reynolds numbers, the disorder can be generated first at the periphery or in the centre and then invades the entire cell.

The domains of existence of all these patterns are summarized in the regime diagram (Re_b, Re_t) of figure 10. We see that the co-rotation flow ($Re_b > 0$, right-hand part of the diagram) is qualitatively the same as the rotor–stator flow (vertical line $Re_b = 0$); the thresholds of instabilities (circles C and positive spirals S^+) are found to increase just with the bottom Reynolds number. By contrast, the counter-rotating case ($Re_b < 0$, left-hand part) is much more rich. The following subsections describe in more detail the three different patterns: axisymmetric propagating vortices §4.1 and positive spirals §4.2 (co- and weak counter-rotation), and negative spirals §4.3 (stronger counter-rotation).

4.1. Axisymmetric propagating vortices

As mentioned in §3.1, in the co-rotation and weak counter-rotation cases, the basic flow is similar to the rotor–stator case, and the sequence of instability patterns is found to be the same. We start with the first instability, the axisymmetric propagating vortices, more simply called circles (C). These circular waves were observed for the first time by Savas (1987) during the spin-down of a rotating cylinder. This author reported that the axisymmetric propagating waves are of class A (Type II), i.e. due to a viscous instability of the inward boundary layer. This result has been recently confirmed theoretically by Fernadez-Feria (2000) for the self-similar flow over an

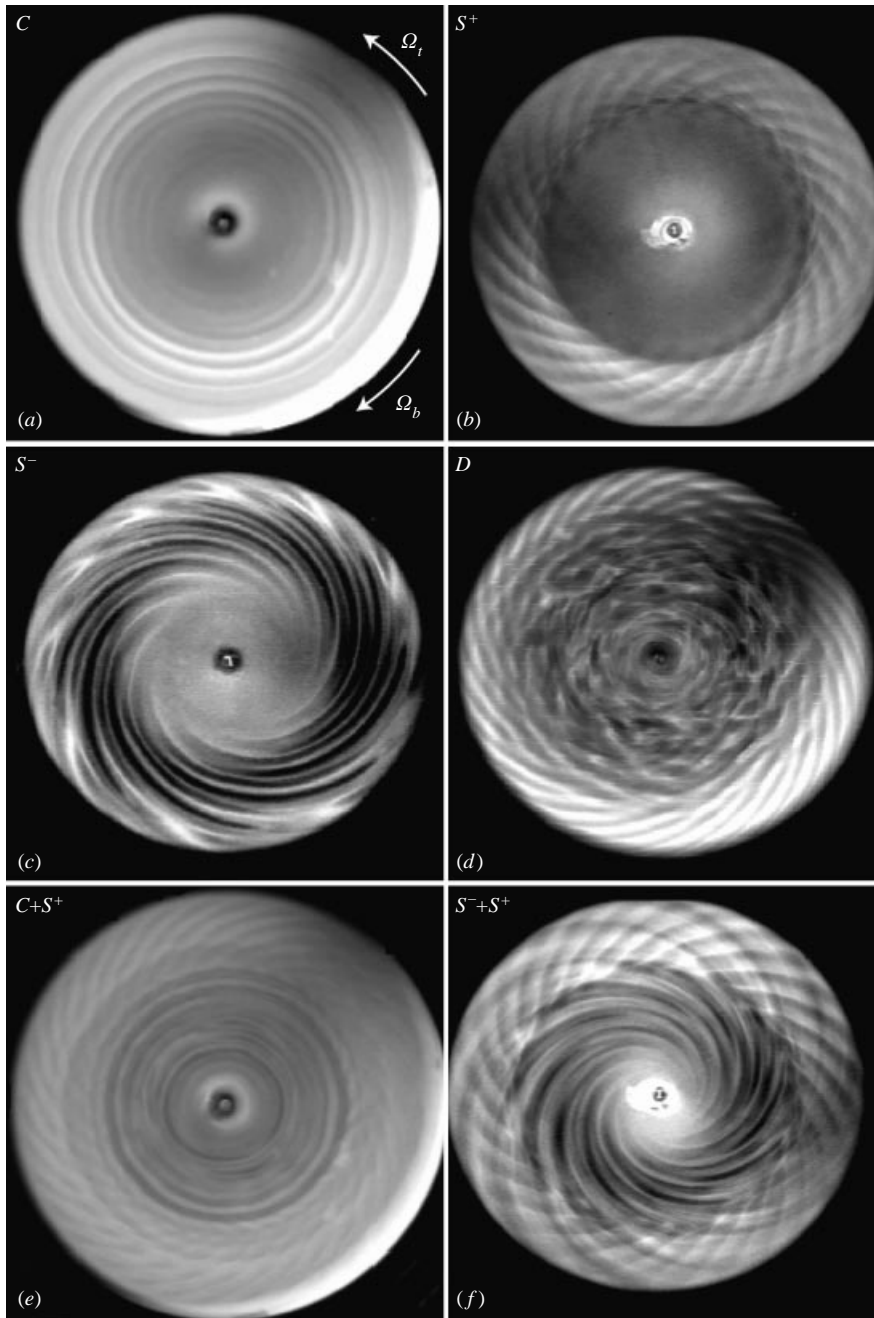


FIGURE 9. Gallery of the different flow patterns: (a) propagating circular vortices C , (b) positive spirals S^+ , (c) negative spirals S^- , (d) disordered flow D , (e) mixing of axisymmetric propagating vortices and positive spirals and (f) mixing of positive and negative spirals. The direction of rotation of the disks is the same for all patterns: the bottom slower disk rotates clockwise while the top faster one rotates anticlockwise.

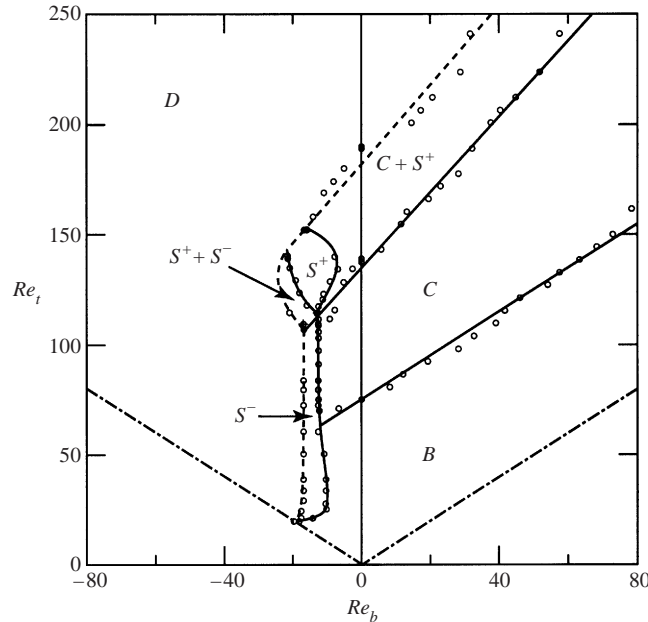


FIGURE 10. Regime diagram of the rotating disk flow for the aspect ratio $R/h = 20.9$. The dot-dashed lines correspond to the first and the second bisectors: $Re_t = Re_b$ (solid-body rotation) and $Re_t = -Re_b$ (exact counter-rotation). The different domains are B (steady axisymmetric basic flow), C (axisymmetric propagating vortices), S^- (negative spirals), S^+ (positive spirals) and D (disorder). The continuous lines define the domain limits, while the dashed lines give a rough estimate of the disorder transition.

infinite disk. Following these authors, the instability we observe should be of Class A, although we are not able to provide any experimental evidence. Such axisymmetric propagating vortices have been studied in detail for the rotor–stator configuration in our previous study (Gauthier *et al.* 1999). As shown in figure 10, the threshold of this instability increases linearly with the rotation of the bottom disk as

$$Re_{t,c} \approx 75 + Re_b,$$

i.e. it depends only on the difference in rotation rates between the top and bottom disks (the relative threshold remains constant in the rotating frame of the bottom disk). This suggests that the relevant parameter of this instability is the shear rate $\sim \Omega_t - \Omega_b$, and the additional global rotation Ω_b just changes the threshold without further stabilization of the flow.

We observe that this instability takes place in the inward boundary layer that develops on the slower rotating disk (for $r > r_m$), in agreement with our previous results in the rotor–stator case. Since the same investigation method has been used, it is only briefly described here. The inward boundary layer behaves as an open flow and then acts as a noise amplifier whose natural frequency is the most amplified one. In order to study such system, one may analyse the flow response to a perturbation of controlled frequency and amplitude. In our set-up this is realized by analysing the flow response to a periodic modulation of the rotation speed of the top disk, which is now: $\Omega_t(t) = \Omega_{t,0} + \Delta\Omega \cos(\omega t)$. The results described hereafter correspond to $\Omega_{t,0} = 4.0 \text{ rad s}^{-1}$ ($Re_t = 175$), $\Omega_b = 1.47 \text{ rad s}^{-1}$ ($Re_b = 66$), $\Delta\Omega/\Omega_{t,0} = 6\%$ and ω in the range 13 to 17 rad s^{-1} .

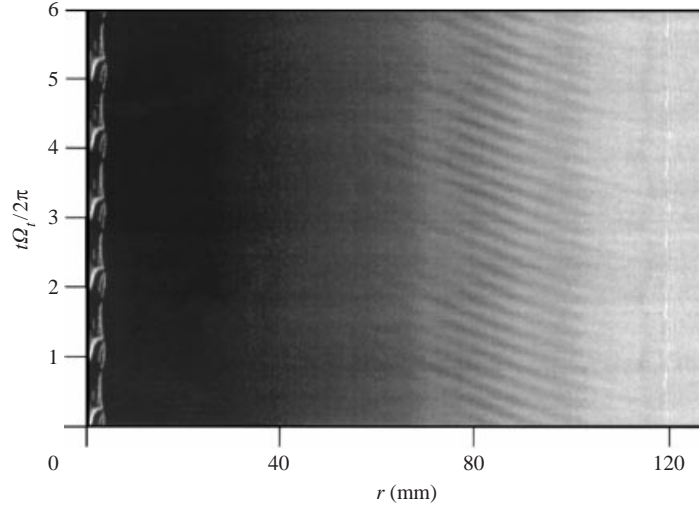


FIGURE 11. Spatiotemporal image of the axisymmetric vortices for $\Omega_{r,0} = 4 \text{ rad s}^{-1}$ ($Re_i = 175$), $\Omega_b = 1.44 \text{ rad s}$, $\omega = 14.5 \text{ rad s}^{-1}$ ($Re_b = 66$).

For each imposed frequency modulation ω , we construct a spatiotemporal image corresponding to the time evolution of the light intensity along a given radius (figure 11). From this spatiotemporal image we extract the temporal power spectrum. As we found that the system amplifies the imposed frequency ω , we use a filter centred around the imposed frequency in order to remove the experimental noise. Then on each spatial line (horizontal lines of constant t in figure 11) the light intensity is: $I(r, t) = I_0(r) \exp(k_r(r)r - \omega t)$. Computing an Hilbert transform (Croquette & Williams 1989) for each horizontal line of the spatiotemporal image gives the local wavenumber $k_r(r)$ and the envelope of the light intensity $I_0(r)$. The light intensity increases from the periphery to a given radius and then decreases towards the centre. The amplitude of the structures and the location of the maximum amplitude both depend on the imposed frequency. As in the rotor–stator case, the system acts as a large band noise amplifier with the most amplified frequency equal to four times the rotation rate of the faster disk. From the envelope $I_0(r)$, one can extract the spatial growth rate k_i using a WKBY approximation (Hinch 1991). Thus, renormalizing both the spatial growth rate and the local wavenumber with the local thickness δ_b of the slower disk boundary layer should collapse the data onto a single curve. Figure 12 shows the non-dimensional spatial growth rate ($k_i \delta_b$) as a function of the non-dimensional local wavenumber ($k_r \delta_b$) for four different frequencies of modulation. As one can see, the band width of the unstable wavenumbers ($0 < k_r \delta_b < 1$) as well as the most unstable wavenumber ($k_r \delta_b \approx 0.6$) are independent of the modulation frequency. The results obtained here are comparable with that previously obtained in the rotor–stator case (Gauthier 1999), where the bandwidth was $0 < k_r \delta_b < 1.5$ and the most unstable wavenumber was $k_r \delta_b \approx 0.5$. In addition, in both studies, the natural frequency of the circular waves is found to be four times the frequency of the faster disk, as also found numerically by Serre *et al.* (2001) for the rotor–stator case.

4.2. Positive spirals

We now turn to the positive spirals (denoted S^+ in figure 9b), present in both the co- and counter-rotating cases. They have been studied extensively in the rotor–stator

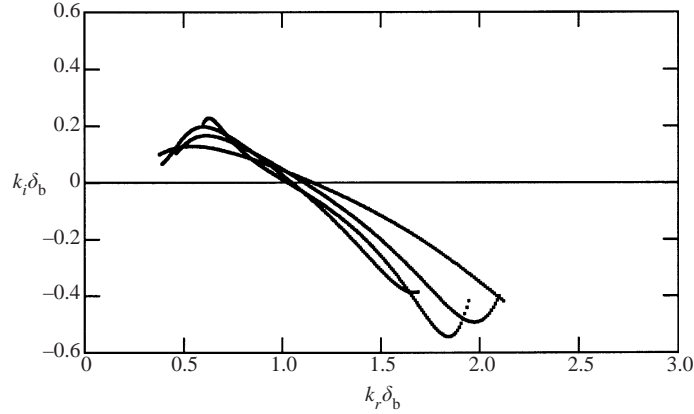


FIGURE 12. Dimensionless spatial growth rate $k_i \delta_b$ of the propagating circles as a function of the dimensionless wavenumber $k_r \delta_b$ for four frequencies of modulation: $\omega/\Omega_{0,t} = 3.2, 3.6, 4$ and 4.2 .

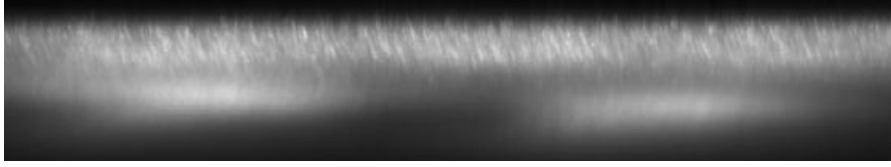


FIGURE 13. Laser sheet visualization of positive spirals for $Re_t = 120$ and $Re_b = 12$. The upper bright line corresponds to the boundary layer of the top disk, and the two bright patches correspond to sections of positive spirals C^+ . The axis of rotation is at the left, the left-hand edge is at $r = 84$ mm and the right-edge $r = 106$ mm.

configuration by Schouveiler, Le Gal & Chauve (1998) and Schouveiler, Le Gal & Chauve (2001). In particular these authors show that, in the rotor–stator configuration, these spirals can appear alone (without circles) if the aspect ratio is large enough ($R/h > 40$, see figure 3 of Schouveiler *et al.* 2001). They give evidence that these positive spirals are due to an instability of the stationary-disk boundary layer. They point out a connection with the study of Hoffman, Busse & Chen (1998), suggesting that an inviscid inflectional instability is responsible for the onset of the positive spirals. As for the axisymmetric propagating vortices, since the flow in co-rotation and weak counter-rotation is qualitatively the same as for the rotor–stator case, we expect the instability mechanism to be similar and thus of Class B (type I). Indeed, our laser sheet visualizations show that the structures are localized in the inward boundary layer attached to the slower disk (see figure 13), in agreement with the findings of Schouveiler *et al.* (1998) in the rotor–stator case.

Positive spirals appear at the periphery and develop towards the centre down to a critical radius. In the co- and weak counter-rotation cases, the critical radius is limited by the existence of axisymmetric propagating vortices, while for stronger counter-rotation this critical radius is found to be the merging radius r_m , defined in §3.1. This observation suggests that positive spirals need a well-defined inward boundary layer to develop, as they disappear at the radius r_m where the inward layer merges with the top-disk outward boundary layer. So positive spirals only exist in the Batchelor-type flow, where a quasi-solid-body rotation takes place between two separate boundary layers.

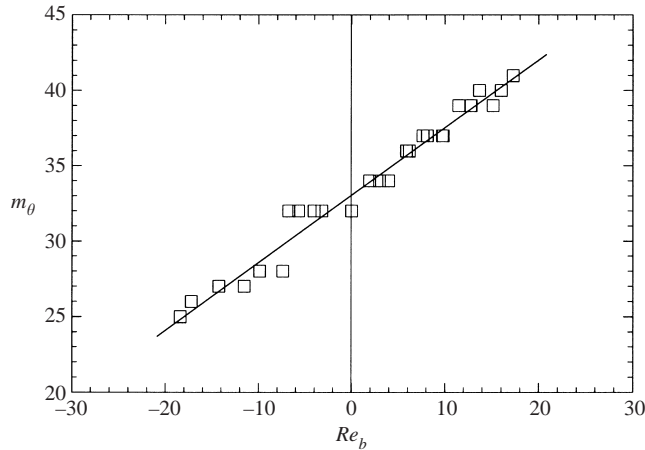


FIGURE 14. Azimuthal wavenumber m_θ of the positive spirals along the onset curve between the C and $C + S^+$ domains (see figure 10) as a function of the bottom Reynolds number.

In the regime diagram of figure 10, we can see that the equation for the line separating domains C and $C + S^+$ is

$$Re_{t,c} \approx 135 + 1.7Re_b$$

for $-18 < Re_b < 60$. We can see that for $Re_b = 0$ (rotor–stator case), our threshold $Re_{t,c} = 135 \pm 8$ is in good agreement with Schouveiler *et al.* (2001) who report a value of $Re = 143 \pm 6$ for the same aspect ratio. For increasing Re_b , the increase of the threshold $Re_{t,c}$ is linear but the slope is larger than one, unlike what was obtained for the axisymmetric propagating vortices: now the mean shear rate $\sim \Omega_t - \Omega_b$ is not the only parameter for this instability, and the additional global rotation Ω_b shifts upward the threshold, i.e. it stabilizes the flow.

A quantity of interest to characterize this instability pattern is the number of spiral arms, or equivalently the azimuthal wavenumber m_θ of its polar Fourier representation. The wavenumber m_θ appears to depend on both the top and bottom Reynolds numbers, and we choose here to focus only on its value at onset along the instability curve $(Re_{t,c}, Re_{b,c})$. It is important to note here that, unlike the negative spirals where higher-order azimuthal wavenumbers may coexist simultaneously with the fundamental mode (see §4.3), we never observe here more than one mode at the same time, even far from the onset. Figure 14 shows that m_θ increases linearly along the onset line, as the bottom Reynolds number is increased. This global evolution is the same in the co- ($Re_b > 0$) and counter- ($Re_b < 0$) rotating cases, supporting our assumption that the instability mechanism for this pattern is essentially the same in the two configurations. With our aspect ratio ($R/h = 20.9$), $m_\theta = 25$ is the minimum wavenumber that can be observed, for $Re_{b,c} \simeq -18$. Due to experimental limitations, we are not able to observe modes beyond $m_\theta = 41$, but we believe that the curve extends further.

We now consider the phase velocity of the positive spirals. We define here the *azimuthal phase velocity* ω_ϕ in the laboratory frame, corresponding to the angular velocity of the global rotation of the spiral pattern. The phase velocity of the onset mode is plotted as a function of the bottom Reynolds number in figure 15. Here again, the continuous evolution suggests that the weak counter-rotation flow behaves like the co-rotation flow. The phase velocity is always positive (anticlockwise), i.e. the

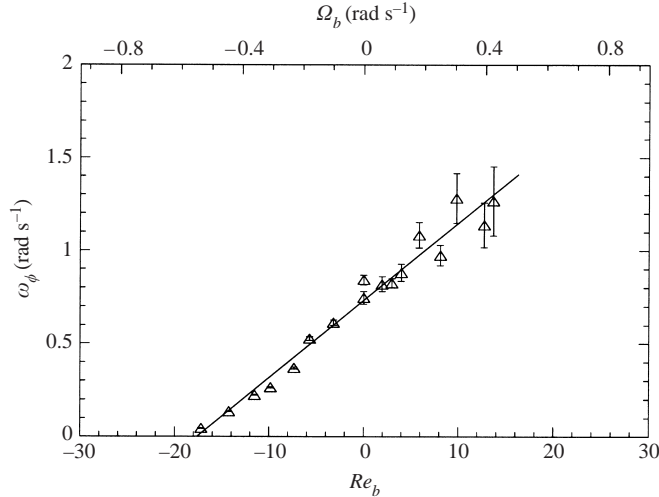


FIGURE 15. Azimuthal phase velocity ω_ϕ of the fundamental mode of the positive spirals as a function of the bottom angular velocity (upper axis) and the bottom Reynolds number (lower axis; $\nu = 1.53 \times 10^{-6} \text{ m}^2 \text{ s}^{-1}$).

positive spirals rotate in the direction of the faster (top) disk, regardless of motion of the bottom one. The evolution is found to be linear, starting from $\omega_\phi = 0$ for $Re_{b,c} \simeq -18$ (here $\Omega_{b,c} = -0.62 \text{ rad s}^{-1}$). The fact that the zero phase velocity coincides with the lower bound of the stability curve seems to be fortuitous, since it is not observed for other aspect ratios.

4.3. Negative spirals

We finally turn to the last instability pattern: when the two disks rotate in opposite directions the first instability leads to another kind of spiral pattern (figure 9c), that we call *negative spirals* since they roll up to the centre in the direction of the slower disk. These negative spirals seem to invade the whole radial extent of the cell, although the light intensity at small radius may become too weak to be seen. Their axial extent can be investigated from the laser sheet visualizations on a meridian plane, as shown in figure 16. The picture reveals a zig-zag lattice of vortices between the upper and lower disk: the negative spirals are not confined to a boundary layer, but rather fill the whole gap between the two disks. In that sense they strongly differ from the axisymmetric propagating vortices and positive spirals described above, which are limited to the inward boundary layer of the slower disk. This observation is supported by the fact that the merging radius r_m , which is the inner bound of the inward boundary layer, does not limit the radial extent of the negative spirals (see figure 9f). The location of the negative spirals is somewhat unexpected in view of the radial structure of the basic axisymmetric laminar flow studied in §3.2: As shown in figure 8, before the onset of the negative spirals, the basic flow has a two-cell recirculating structure with a stagnation circle on the (slower) bottom disk. Above the onset of the negative spirals, the flow is no longer axisymmetric but we observe that the stagnation circle remains, meaning that the radial component of the flow is not much affected by the axisymmetry breaking: the negative spirals pattern invades the whole cell, in both radial and axial directions, regardless of the position of the stagnation circle. The fact that negative spirals exist in regions where the radial recirculating flow can be either

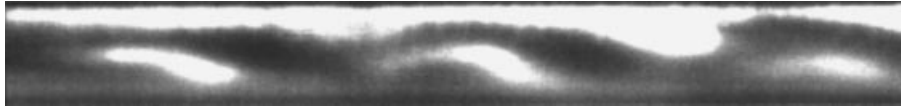


FIGURE 16. Radial laser sheet visualization of negative spirals for $Re_t = 85$ and $Re_b = -16$. The left-hand edge is at $r \approx 50$ mm and the right-hand edge at $r \approx 90$ mm.

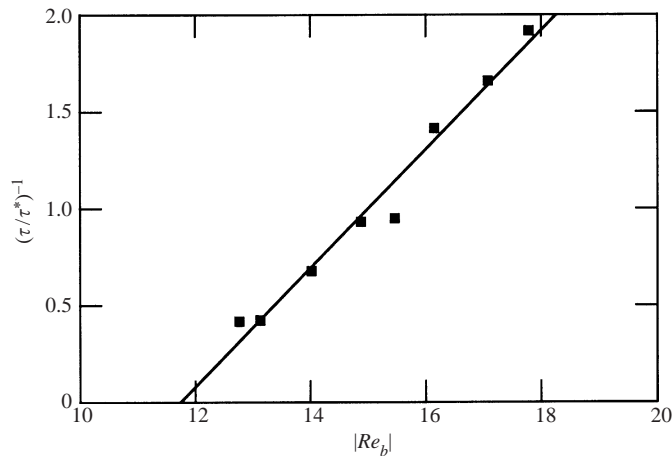


FIGURE 17. Inverse of the growth time τ of negative spirals, normalized with the viscous diffusion time $\tau^* = h^2/\nu$, as a function of the bottom Reynolds number Re_b , for $Re_t = 54$.

outward or inward is a hint that the instability mechanism is not of cross-flow type (Class B).

Perhaps the most striking characteristic of the negative spirals is their very large growth time: when the onset is carefully approached from below, this growth time can exceed 15 minutes (using water as the working fluid), i.e. more than 30 turnover times of the slower (bottom) disk. Such large growth time strongly contrasts with the positive spirals and circles, which appear almost instantaneously compared to the rotation timescale. Since in the vicinity of the threshold the growth time is expected to diverge as $|Re_b - Re_{b,c}|^{-1}$, plotting the inverse of the growth time $1/\tau$ for a given (faster) top Reynolds number as a function of Re_b allows an accurate determination of the threshold $Re_{b,c}$. Figure 17 shows, for $Re_t = 54$, the inverse of the non-dimensional growth time τ/τ^* , where $\tau^* = h^2/\nu$ denotes the viscous diffusion time, as a function of Re_b . Indeed, the evolution appears to be linear, and the extrapolation $1/\tau \rightarrow 0$ allows the threshold to be determined. No hysteresis has been found in this transition, giving evidence that the axisymmetry is broken via a supercritical Hopf bifurcation. The threshold $Re_{b,c}$, plotted as a function of Re_t in figure 18, is found to evolve very slightly with the top Reynolds number, defining the existence domain of negative spirals in the ‘regime diagram’. As Re_t is increased, the critical bottom Reynolds number first slightly decreases down to a minimum ($Re_{b,c} \approx 11 \pm 0.5$ for $Re_t \approx 40$) and then increases up to 16, showing that the bifurcation is not only related to the shear induced by the differential disks rotation.

As for the positive spirals, an important property of this spiral pattern is its azimuthal wavenumber. However, it is worth pointing out that, unlike the positive spirals, higher-order modes quickly superimpose on the fundamental one, even very close above the onset. In this case, each mode rotates with its own azimuthal phase

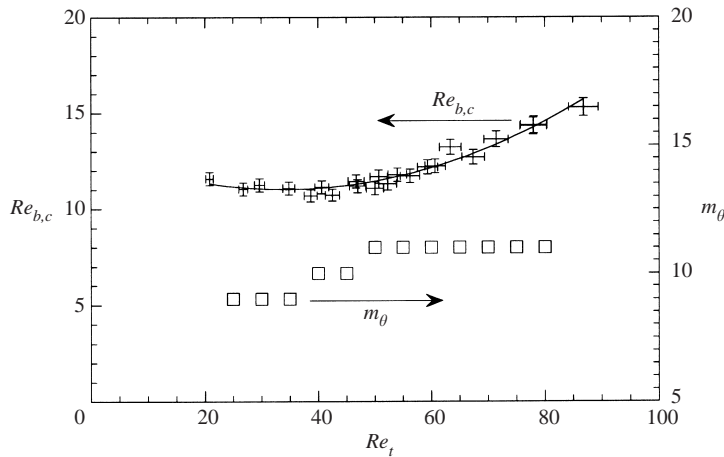


FIGURE 18. Critical bottom Reynolds number $Re_{b,c}$ (left axis) and azimuthal mode m_{θ} at onset (right axis) of the negative spirals as a function of the top Reynolds number.

velocity, leading to a slowly rotating modulation of the pure spiral pattern. Here again, we will only focus on the fundamental (lower order) mode at onset, which can be simply viewed as the number of spiral arms.

At threshold, after the appearance of the structures, we observe that the azimuthal wavenumber evolves through a cascade of rearrangements to reach a stable mode. For instance, for $Re_t = 50$ and slowly increasing Re_b up to its critical value $Re_{b,c} \approx 11.5$, we first observe a transient mode $m_{\theta} = 13$, which decays within tens of minutes down to its stable fundamental state $m_{\theta} = 11$. We note that the timescale for this rearrangement is large, of the same order as the growth time of the initial mode. The azimuthal wavenumber m_{θ} of the fundamental mode (at onset) is plotted in figure 18 (right axis) as a function of the top Reynolds number (each point of this figure is obtained after the decay of all transient modes). As the top (larger) Reynolds number is increased, and keeping the bottom Reynolds number at its corresponding onset value $Re_{b,c}$, m_{θ} is found to increase from 9 to 11. On the other hand, going above the onset by keeping Re_t constant and slightly increasing Re_b , the situation is much more complex: as soon as Re_b is increased by 5% from $Re_{b,c}$, a secondary mode appears. This mode is clearly not an harmonic of the fundamental one (it ranges between 14 and 19), and the number of spiral arms is no longer defined. Increasing further the bottom Reynolds number ($|Re_b| > 18$), other higher-order modes appear, rapidly leading to a disordered pattern.

We finally look to the phase velocity of the negative spirals. Figure 19 shows the evolution of the azimuthal phase velocity ω_{ϕ} of the fundamental mode in the laboratory frame as a function of the top Reynolds number. We first observe that the sign of ω_{ϕ} changes, i.e. the rotation of the pattern is not simply related to the direction of either disk. The mode $m_{\theta} = 9$ ($Re_t < 40$) is associated with negative (clockwise) phase velocity, while the mode $m_{\theta} = 11$ ($Re_t > 50$) has positive (anticlockwise) phase velocity. It means that, at small Re_t , the pattern rotates in the direction of the slower (bottom) disk, with the convex side of the spiral arms in the direction of motion, while at higher Re_t it moves with the top (faster) disk with the concave side ahead. This situation contrasts with the positive spirals, for which the azimuthal phase velocity is always of constant sign, corresponding to a motion of the spiral arms with the concave side ahead. We note that this change of sign for negative spirals occurs at

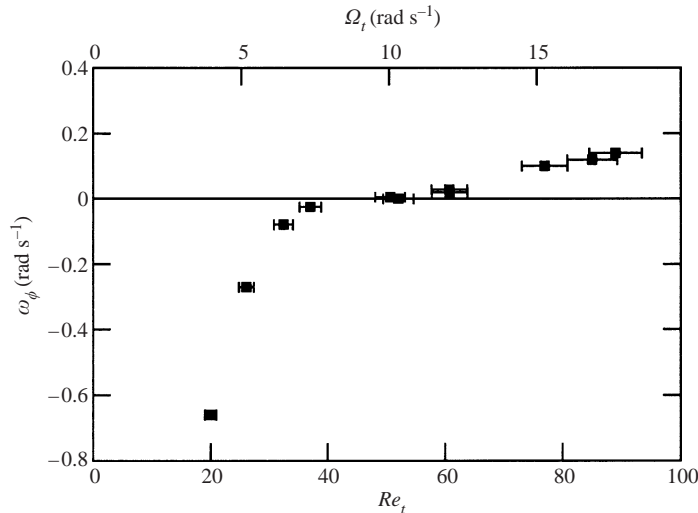


FIGURE 19. Azimuthal phase velocity ω_ϕ of the negative spirals at threshold as a function of the top Reynolds number Re_t (bottom axis) and corresponding angular velocity Ω_t (top axis).

the minimum of the domain boundary ($Re_t \approx 50 \pm 10$, $Re_b \simeq -11$). In the vicinity of this minimum, we note that the phase velocity is found to be very small (typically 1% of the faster disk rotation rate, with almost no variation with Re_t), i.e. the pattern seems to be almost at rest in the laboratory frame.

5. Discussion and conclusion

In this article, we have investigated experimentally the flow and its instabilities between two parallel co- or counter-rotating disks with an enclosing cylinder attached to the faster (top) disk, for an aspect ratio $R/h = 20.9$. Special attention has been paid to the basic laminar flow, in order to obtain more insight into the onset of the different instability patterns and their region of existence. Three different kinds of patterns are reported and described in detail: axisymmetric propagating vortices, positive spirals and negative spirals. The first two ones, which are both present in co- and weak counter-rotating flows, have been previously investigated in the rotor–stator configuration in our experimental set-up (Gauthier *et al.* 1999) as well as by other authors (Schouveiler *et al.* 2001; Serre, Crespo de Arco & Bontoux 2001). By contrast, the negative spirals are specific to the counter-rotating flow, and are described here for the first time.

When the disks are co-rotating or when the counter-rotation is weak ($-11 < Re_b < 0$) the basic flow is found to be of Batchelor type (separated boundary layers) above a given radius and of torsional Couette type below. No qualitative difference is found when compared with the rotor–stator configuration, and the instabilities encountered are the same: axisymmetric propagating vortices and positive spirals. Azimuthal wavenumbers and phase velocities at onset have been measured for the positive spirals, showing a continuous evolution from counter- to co-rotation. These patterns occur in the slower-disk inward boundary layer, while the faster-disk boundary layer as well as the core are found to remain stable in our range of Reynolds numbers. For this reason, the radial extent of these patterns is limited by the merging radius r_m . We have shown that the behaviour of the axisymmetric propagating

vortices for $s \neq 0$ is the same as in the rotor–stator case studied previously (Gauthier *et al.* 1999). In particular, it is worth noting that the additional global rotation for $s \neq 0$ only moves the instability threshold of the circles linearly, without further stabilization of the flow. This situation is remarkable, since the basic flow is clearly affected by additional global rotation. By contrast, the positive spirals are shown to be stabilized by the global rotation, since their instability threshold is moved more as the rotation is increased.

When the disks rotate in opposite directions a new instability pattern is reported, called negative spirals. The instability leading to this new pattern corresponds to a supercritical Hopf bifurcation. Negative spirals significantly differ from circles and positive spirals in the sense that they extend over the whole cell in both the radial and axial directions. Their apparent insensitivity to the merging radius r_m is evidence that they are not confined in one boundary layer, unlike the circles and positive spirals, and that the instability mechanism is not of cross-flow type. We thus believe that negative spirals arise from a shear instability in the bulk of the flow. We further observed that negative spirals may coexist with positive spirals, but not with propagating circles. This suggests that the instability leading to the propagating circles can only take place in an axisymmetric region of the flow. We have measured the azimuthal wavenumber and phase velocity of negative spirals, and showed that the fundamental mode is essentially controlled by the larger Reynolds number. Going slightly above the onset of negative spirals, disorder and turbulence quickly arise after few secondary instabilities.

Recently Lopez *et al.* (2002) reported, from both experimental and numerical investigations, azimuthal modulation of the counter-rotating flow for an aspect ratio $R/h = 2$. Depending on the counter-rotation ratio, these authors report azimuthal modes $m_\theta = 4$ and 5. These numbers should be compared to the modes $m_\theta = 9, 10$ and 11 that we observe for the negative spirals with $R/h = 20.9$. In spite of the large aspect ratio difference, it raises the issue of a possible continuity between their instability and our negative spirals. According to these authors (see also Lopez 1998), their instabilities arise from an inward jet-like shear layer. This free shear layer originates from the separation of the inward boundary layer due to the stagnation circle present at $s < -0.2$. However, we observe that negative spirals extend both below and above the stagnation circle, and both in the separated boundary layers region ($r > r_m$) and in the torsional Couette region ($r < r_m$). At this point, it is not clear whether or not our observations support the instability mechanism proposed by these authors, at least for the aspect ratio we investigate. More experiments, with different aspect ratios, have to be performed in order to clarify this issue.

The authors wish to thank G. Michon and B. Truchot for experimental helps, and O. Daube for fruitful discussions.

REFERENCES

- BATCHELOR, G. K. 1951 Note on a class of solutions of the Navier–Stokes equations representing steady rotationally–symmetric flow. *Q. J. Mech. Appl. Maths* **4**, 29–41.
- BÖDEWADT, U. T. 1940 Die Drehströmung über festem Grund. *Z. Angew. Math. Mech.* **20**, 241–253.
- BRADY, J. F. & DURLOFSKY, L. 1987 On rotating disk flow. *J. Fluid Mech.* **175**, 363–393.
- CROQUETTE, V. & WILLIAMS, H. 1989 Nonlinear waves of the oscillatory instability on finite convective rolls. *Physica D* **37**, 300–314.
- DIJKSTRA, D. & VAN HEIJST, G. J. F. 1983 The flow between finite rotating disks enclosed by a cylinder. *J. Fluid Mech.* **128**, 123–154.

- EKMAN, V. W. 1905 On the influence of the Earth's rotation on ocean currents. *Arkiv. Mat. Astr. Fys. Bd* 2 **11**, 1–52.
- FALLER, A. J. & KAYLOR, R. E. 1966 Numerical study of the instability of the laminar Ekman boundary layer. *J. Atmos. Sci.* **23**, 466–480.
- FERNANDEZ-FERIA, R. 2000 Axisymmetric instabilities of Bödewadt flow. *Phys. Fluids* **12**, 1730–1739.
- GAUTHIER, G. 1998 Etude expérimentale des instabilités de l'écoulement entre deux disques. PhD thesis, Université Paris XI.
- GAUTHIER, G., GONDRET, P. & RABAUD, M. 1998 Motions of anisotropic particles: application to visualization of three-dimensional flows. *Phys. Fluids* **10**, 2147–2154.
- GAUTHIER, G., GONDRET, P. & RABAUD, M. 1999 Axisymmetric propagating vortices in the flow between a stationary and a rotating disk enclosed by a cylinder. *J. Fluid Mech.* **386**, 105–126.
- GREENSPAN, H. P. 1968 *The Theory of Rotating Fluids*. Cambridge University Press.
- GREGORY, N., STUART, J. T. & WALKER, W. S. 1955 On the stability of three dimensional boundary layers with application to the flow due to a rotating disk. *Phil. Trans. R. Soc. Lond.* **248**, 155–199.
- HINCH, J. 1991 *Perturbation Methods*. Cambridge University Press.
- HOFFMAN, N., BUSSE, F. H. & CHEN, W. L. 1998 Transitions to complex flows in the Ekman–Couette layer. *J. Fluid Mech.* **366**, 311–331.
- VON KÁRMÁN, T. 1921 Laminar und turbulente reibung. *Z. Angew. Math.* **1**, 233–252.
- LOPEZ, J. M. 1998 Characteristics of endwall and sidewall boundary layers in a rotating cylinder with a differentially rotating endwall. *J. Fluid Mech.* **359**, 49–79.
- LOPEZ, J. M., HART, J. E., MARQUES, F., KITTELMAN, S. & SHEN, J. 2002 Instability and mode interactions in a differentially driven rotating cylinder. *J. Fluid Mech.* **462**, 383–409.
- NORE, C., TUCKERMAN, L. S., DAUBE, O. & XIN, S. 2003 The 1:2 mode interaction in exactly counter-rotating von Kármán swirling flow. *J. Fluid Mech.* (in press).
- RANDRIAMAMPINANINA, A., ELENA, L., FONTAINE, J.-P. & SCHIESTEL, R. 1997 Numerical prediction of laminar, transitional and turbulent flows in shrouded rotor-stator systems. *Phys. Fluids* **9**, 1696–1713.
- ROGERS, M. H. & LANCE, G. N. 1960 The rotationally symmetric flow of a viscous fluid in the presence of an infinite rotating disk. *J. Fluid. Mech.* **7**, 617–631.
- SAVAS, Ö. 1985 On flow visualization using reflective flakes. *J. Fluid Mech.* **152**, 235–248.
- SAVAS, Ö. 1987 Stability of Bödewadt flow. *J. Fluid Mech.* **183**, 77–94.
- SCHOUVEILER, L., LE GAL, P. & CHAUVE, M.-P. 1998 Stability of a travelling roll system in a rotating disk flow. *Phys. Fluids* **10**, 2695–2697.
- SCHOUVEILER, L., LE GAL, P. & CHAUVE, M.-P. 2001 Instabilities of the flow between a rotating and stationary disk. *J. Fluid Mech.* **443**, 329–350.
- SERRE, E., CRESPO DEL ARCO, E. & BONToux, P. 2001 Annular and spiral patterns in flows between rotating and stationary discs. *J. Fluid Mech.* **434**, 65–100.
- SIRIVAT, A. 1991 Stability experiment of flow between a stationary and a rotating disk. *Phys. Fluids A* **3**, 2664–2671.
- STEWARTSON, K. 1953 On the flow between two rotating coaxial disks. *Proc. Camb. Phil. Soc.* **49**, 333–341.
- SZERI, A. Z., GIRON, A., SCHNEIDER, S. J. & KAUFMAN, H. N. 1983 Flow between rotating disks. Part 2. Stability. *J. Fluid Mech.* **134**, 133–154.
- ZANDBERGEN, P. J. & DIJKSTRA, D. 1987 Von Kármán swirling flows. *Annu. Rev. Fluid Mech.* **19**, 465–491.